The Maximum Mass-loss Efficiency for a Photoionization-driven Isothermal Parker Wind

Shreyas Vissapragada[1] , Heather A. Knutson[1] , Leonardo A. dos Santos[2,3] , Lile Wang[4] , and Fei Dai[1]

[1] Division of Geological and Planetary Sciences, California Institute of Technology, 1200 East California Blvd, Pasadena, CA 91125, USA; svissapr@caltech.edu
[2] Space Telescope Science Institute, 3700 San Martin Drive, Baltimore, MD 21218, USA
[3] Observatoire astronomique de l'Université de Genève, Chemin Pegasi 51, 1290 Versoix, Switzerland
[4] Center for Computational Astrophysics, Flatiron Institute, New York, NY 10010, USA

Abstract

Observations of present-day mass-loss rates for close-in transiting exoplanets provide a crucial check on models of planetary evolution. One common approach is to model the planetary absorption signal during the transit in lines like He I 10830 with an isothermal Parker wind, but this leads to a degeneracy between the assumed outflow temperature T_0 and the mass-loss rate $\dot{M}$ that can span orders of magnitude in $\dot{M}$. In this study, we re-examine the isothermal Parker wind model using an energy-limited framework. We show that in cases where photoionization is the only heat source, there is a physical upper limit to the efficiency parameter ε corresponding to the maximal amount of heating. This allows us to rule out a subset of winds with high temperatures and large mass-loss rates as they do not generate enough heat to remain self-consistent. To demonstrate the utility of this framework, we consider spectrally unresolved metastable helium observations of HAT-P-11b, WASP-69b, and HAT-P-18b. For the former two planets, we find that only relatively weak ($\dot{M} \lesssim 10^{11.5}$ g s^{-1}) outflows can match the metastable helium observations while remaining energetically self-consistent, while for HAT-P-18b all of the Parker wind models matching the helium data are self-consistent. Our results are in good agreement with more detailed self-consistent simulations and constraints from high-resolution transit spectra.

1. Introduction

A majority of the extrasolar planets discovered by transit surveys orbit close to their host stars and are subjected to intense irradiation. The incident flux received by these planets can remove their atmospheres if the heating is large compared to the planet's gravitational potential. Indeed, we see evidence for atmospheric escape in the radius–period distribution of close-in planets (the "evaporation valley") observed by Kepler and K2 (Fulton et al. 2017; Fulton & Petigura 2018; Van Eylen et al. 2018; Hardegree-Ullman et al. 2020). We can quantify the present-day mass loss rates of the most favorable transiting planets by measuring the amount of absorption during the transit in spectral lines where outflowing material becomes opaque. To date, atmospheric outflows have been detected using Lyα (e.g., Vidal-Madjar et al. 2003), Hα (e.g., Yan & Henning 2018), metal lines (e.g., Vidal-Madjar et al. 2004), and metastable helium (e.g., Spake et al. 2018).

The upper atmospheres of planets are engines that turn light into heat. This heating drives hydrodynamic escape by lifting material out of the planet's gravitational potential well. We can use this concept to calculate an "energy-limited" mass loss rate, as first done (albeit in the context of highly conductive

atmospheres) by Watson et al. (1981):

$$\dot{M} = \frac{\varepsilon \pi R_{\mathrm{XUV}}^2 F_{\mathrm{XUV}}}{K G M_{\mathrm{P}}/R_{\mathrm{P}}}. \tag{1}$$

The numerator of this equation is an estimate for the heating rate of the planet (in erg s^{-1}), where the stellar high-energy flux F_{XUV} (in erg s^{-1} cm^{-2}) impinges on a cross-sectional area πR_{XUV}^2 of the planet, heating it with efficiency ε. The denominator is the gravitational potential (in erg g^{-1}), with a correction factor K to account for the fact that atoms need only be lifted past the Roche lobe to escape the planet (Erkaev et al. 2007):

$$K = 1 - \frac{3}{2}\left(\frac{R_{\mathrm{P}}}{R_{\mathrm{Roche}}}\right) + \frac{1}{2}\left(\frac{R_{\mathrm{P}}}{R_{\mathrm{Roche}}}\right)^3. \tag{2}$$

For small planet-to-star mass ratios, the Roche radius can be written as:

$$R_{\mathrm{roche}} \approx a\left(\frac{M_{\mathrm{P}}}{3M_\star}\right)^{1/3}. \tag{3}$$

The limitations of this formalism are well-documented (e.g., Murray-Clay et al. 2009; Salz et al. 2016a, 2016b; Kubyshkina et al. 2018; Owen 2019; Krenn et al. 2021). Detailed hydrodynamical models show that the efficiency ε depends strongly on a number of factors, including the planetary mass, radius, atmospheric composition, assumed heating processes, and stellar spectrum (Owen & Jackson 2012; Shematovich et al. 2014). Despite these drawbacks, this equation offers a convenient way to predict mass loss without expensive computational modeling, and it has been used extensively to

model the Kepler evaporation valley (Lopez & Fortney 2013; Owen & Wu 2013, 2017).

The energy-limited framework has also recently been used to interpret measurements of metastable helium absorption from close-in transiting gas giant planets (Lampón et al. 2021a, 2021b). Helium observations are typically modeled using an isothermal Parker wind (parameterized by an assumed outflow temperature T_0 and mass-loss rate $\dot{M}$) coupled to a set of photoionization equations that can be solved for the He level populations as a function of altitude (Oklopčić & Hirata 2018). The photoionized Parker wind model is faster to compute than expensive self-consistent 3D simulations (Wang & Dai 2021a, 2021b), making it easier to map out the parameter spaces that fit measurements (and non-detections) of absorption in the metastable helium triplet (Mansfield et al. 2018; Gaidos et al. 2020a, 2020b; Hirano et al. 2020; Ninan et al. 2020; Vissapragada et al. 2020; Krishnamurthy et al. 2021; Paragas et al. 2021). However, there is a degeneracy between $\dot{M}$ and T_0 in the Parker wind model, which can lead to uncertainties in $\dot{M}$ that span multiple orders of magnitude. This is particularly problematic for lower signal-to-noise and/or spectroscopically unresolved observations of helium absorption where the temperature of the outflow is unconstrained by the data.

In this work, we show that the $\dot{M}$–T_0 degeneracy in helium observations can be partially resolved because there is an upper limit to the efficiency of an energy-limited H/He outflow corresponding to the maximal amount of heating from photoionization. In Section 2, we derive an expression for $\varepsilon_{\mathrm{max}}$ in a lossless isothermal wind, i.e., a wind in which radiative cooling is negligible. We show that this expression can be used to define a bounded region in the $\dot{M}$–T_0 plane, beyond which there is not enough heat to power the outflow. In Section 3 we use this framework to resolve the $\dot{M}$–T_0 degeneracy in previous modeling of metastable helium absorption from HAT-P-11b, WASP-69b, and HAT-P-18b. Finally, we offer some concluding thoughts in Section 4.

2. The Maximum Mass-loss Efficiency

We first calculate the maximal outflow efficiency ε for a lossless isothermal wind, assuming that the heat source is photoionization of H and He. Then, we use the maximum efficiency to trace out a critical region on the $\dot{M}$–T_0 plane, which can be used to assess energetic self-consistency. Because constants can always be absorbed into the efficiency ε, we will make the common arbitrary definition $R_{\mathrm{XUV}} \equiv R_{\mathrm{p}}$ in Equation (1) and absorb the constant $(R_{\mathrm{XUV}}/R_{\mathrm{p}})^2$ into ε, admitting the somewhat awkward possibility that $\varepsilon > 1$ if $R_{\mathrm{XUV}} \gg R_{\mathrm{p}}$. We note that other authors have proceeded by fixing ε and calculating R_{XUV} instead (e.g., Erkaev et al. 2007; Salz et al. 2016a; Kubyshkina et al. 2018). This calculation could be restructured for R_{XUV} or the product $\varepsilon R_{\mathrm{XUV}}^2$, but we choose to work with the efficiency term because this is typically the free parameter assumed in planetary population studies. We also note that varying authors have different definitions of the "efficiency" term in the context of planetary wind. For example, Shematovich et al. (2014) defines it as the ratio of the local heating rate to the radiative input (treating the cooling processes separately), which is adopted by Erkaev et al. (2007) and Kubyshkina et al. (2018), whereas Salz et al. (2016b) includes the cooling rate explicitly. Throughout this work, when we refer to the "efficiency," we are referring explicitly to the ε term in Equation (1).

2.1. An Upper Limit to the Mass-loss Efficiency

To compute ε, we begin by writing down the equation for energy balance in the wind (Lamers & Cassinelli 1999; Erkaev et al. 2007):

$$\dot{M}\left(\frac{KGM_{\mathrm{p}}}{R_{\mathrm{p}}} + \frac{\Delta v^2}{2} + \frac{5}{2}\frac{k\Delta T}{\mu m_{\mathrm{H}}}\right) = \iiint \Gamma_{\mathrm{net}}dV, \qquad (4)$$

where $\dot{M}$ is the mass-loss rate of the planet, K is as defined in Equation (2), Δv is the difference in outflow velocity between R_{p} and R_{Roche}, ΔT is the difference in temperature between R_{p} and R_{Roche}, and μ is the mean particle mass of the outflow. The terms on the left-hand side correspond to the difference in gravitational potential energy, kinetic energy, and enthalpy (for a monatomic outflow) between the planetary radius and the Roche lobe. On the right-hand side is the integrated net heating rate per unit volume, with $\Gamma_{\mathrm{net}} = \Gamma - \Lambda$ (where Γ and Λ are the heating and cooling rates, respectively) in erg s^{-1} cm^{-3}.

In this work we only consider isothermal winds where $\Delta T = 0$ and assume that the kinetic energy term is small. In the Parker wind model, material is accelerated to velocities on the order of the sound speed at the Roche lobe. This means that $\Delta v \sim 10^6$ cm s^{-1} (e.g., Murray-Clay et al. 2009; Oklopčić & Hirata 2018) and $(\Delta v)^2/2 \sim 5 \times 10^{11}$ erg g^{-1}, whereas the gravitational potential term is $\gtrsim 10^{12}$ erg g^{-1} for all of the planets considered in this work. These are the same assumptions made by Erkaev et al. (2007) to reproduce the energy-limited mass loss expression from Watson et al. (1981) in Equation (1).

With these assumptions, and using Equation (1) to substitute for the gravitational potential term, we have:

$$\varepsilon \pi R_{\mathrm{p}}^2 F_{\mathrm{XUV}} = \iiint (\Gamma - \Lambda)dV. \qquad (5)$$

This simply reflects our assumption that the numerator of Equation (1) is a proxy for the total heating experienced by the planet. We then calculate ε for an atmosphere where radiative losses are negligible; that is, one where all heating goes into driving the outflow and $\Lambda \ll \Gamma$. This corresponds to:

$$\varepsilon_{\mathrm{max}} \pi R_{\mathrm{p}}^2 F_{\mathrm{XUV}} = \iiint_H \Gamma dV, \qquad (6)$$

where $\varepsilon_{\mathrm{max}}$ is the maximum mass-loss efficiency and H denotes the dayside hemisphere where the heating occurs. If we assume that all heating comes from photoionization, we can write the total heating rate as a sum of heating rates for each photoprocess of interest (e.g., Osterbrock & Ferland 2006):

$$\Gamma = \sum_i \Gamma_i \qquad (7)$$

$$= \sum_i n_{i,r} \int_{\min(\nu_i)}^{\infty} (h\nu - h\nu_i)$$
$$\times \frac{F_\nu \cos(\theta) \exp(-\tau_{\nu,r})}{h\nu} \sigma_{\nu,i} d\nu. \qquad (8)$$

In this equation, $h\nu$ denotes the photon energy. The subscript i denotes different photoprocesses (for instance, hydrogen photoionization), the subscript ν denotes a quantity that varies with frequency, and the subscript r denotes one that varies with radius. The number density profile of the species being photoionized is $n_{i,r}$, the ionization threshold for the process is

$h\nu_i$, and $h\nu - h\nu_i$ is the maximum yield per photoprocess. For example, a photon with energy $h\nu = 20$ eV yields 6.4 eV when ionizing a hydrogen atom out of its ground state ($h\nu_H = 13.6$ eV). $F_\nu \cos(\theta) \exp(-\tau_{\nu,r})$ is the spectrum of radiation reaching radius r from the center of the planet and latitude θ with respect to the substellar point in erg s^{-1} cm^{-2} Hz^{-1}. Finally, $\sigma_{\nu,i}$ is the frequency-dependent cross-section for photoprocess i. The frequency integral is taken from the minimum photoionization threshold over all relevant photoprocesses $\min(\nu_i)$ to allow for a consistent definition of F_{XUV}.

The optical depth term is defined as:

$$\tau_{\nu,r} = \sum_i \sigma_{i,\nu} \int_r^\infty n_{i,r} dr. \qquad (9)$$

This definition implicitly assumes that the optical depth reaches a large value at R_p. For high-energy photons where the photoionization cross-sections are small this condition may not always be satisfied, implying that photons can freely reach this depth. However, these photons cannot pass through the planet, and their energy must be deposited somewhere. We assume that they participate in the energy balance of the lower atmosphere at $R \sim R_p$, and that they do not heat the outflow.

We collect the photon energy terms into a normalized yield term η_ν:

$$\eta_\nu = \frac{h\nu - h\nu_i}{h\nu} = 1 - \frac{\nu_i}{\nu}. \qquad (10)$$

In reality, this is an upper limit on the yield. We have assumed that the photoelectrons resulting from ionization transform all of their energy into heat, but they can also excite or ionize other atoms (Murray-Clay et al. 2009; Shematovich et al. 2014). By neglecting these minor energy deposition channels, we obtain a slightly more generous upper limit than we would otherwise. With the yield term now defined, we can write the total heating rate as:

$$\Gamma = \sum_i n_{i,r} \int_{\min(\nu_i)}^\infty \eta_\nu F_\nu \cos(\theta) \exp(-\tau_{\nu,r}) \sigma_{\nu,i} d\nu. \qquad (11)$$

We integrate this equation over the dayside hemisphere (for the geometry of the integral see e.g., Chapter 2 of Seager 2010):

$$\iiint_H \Gamma dV = \int_0^{2\pi} \int_0^{\pi/2} \int_{R_p}^{R_{Roche}} \Gamma r^2 \sin\theta dr d\theta d\phi \qquad (12)$$

$$= \pi \int_{R_p}^{R_{Roche}} r^2 \sum_i n_{i,r}$$

$$\times \int_{\min(\nu_i)}^\infty \eta_\nu F_\nu \exp(-\tau_{\nu,r}) \sigma_{\nu,i} d\nu dr. \qquad (13)$$

We then substitute Equation (13) into Equation (6), where the factors of π cancel. Noting that F_{XUV} can be written as:

$$F_{XUV} = \int_{\min(\nu_i)}^\infty F_\nu d\nu, \qquad (14)$$

we arrive at:

$$\varepsilon_{max} = \frac{1}{R_p^2} \int_{R_p}^{R_{Roche}} r^2$$

$$\times \sum_i n_{i,r} \frac{\int_{\min(\nu_i)}^\infty \eta_\nu F_\nu \exp(-\tau_{\nu,r}) \sigma_{\nu,i} d\nu}{\int_{\min(\nu_i)}^\infty F_\nu d\nu} dr. \qquad (15)$$

2.2. Heating Cross-sections

We can define the ratio of frequency integrals in Equation (15) as a cross section weighted by the stellar spectrum and heating efficiency for photoprocess i. We call this the "heating cross-section," and note that the optical depth dependence causes it to vary with radius:

$$\bar{\sigma}_{i,r} = \frac{\int_{\min(\nu_i)}^\infty \eta_\nu F_\nu \exp(-\tau_{\nu,r}) \sigma_{\nu,i} d\nu}{\int_{\min(\nu_i)}^\infty F_\nu d\nu}. \qquad (16)$$

To calculate this heating cross-section, we require a stellar spectrum and a frequency-dependent cross-section for each photoprocess. For the spectrum, we use the v2.2 panchromatic SEDs at 1 Å binning from the MUSCLES survey (France et al. 2016; Loyd et al. 2016; Youngblood et al. 2016). For the hydrogen photoionization cross-section, we use (e.g., Osterbrock & Ferland 2006):

$$\sigma_i(\nu) = \sigma_{\nu_i} \frac{\exp\left(4 - 4\frac{\tan^{-1}\epsilon}{\epsilon}\right)}{1 - \exp(-2\pi/\epsilon)} \left(\frac{\nu_i}{\nu}\right)^4,$$
$$\nu > \nu_i, \qquad (17)$$

where $\epsilon = \nu/\nu_i - 1$. The threshold energy for neutral hydrogen photoionization is $h\nu_H = 13.6$ eV, and the cross-section at this threshold is $\sigma_{\nu_H} = 6.3 \times 10^{-18}$ cm^{-2}. We also consider heat generated by the photoionization of ionized helium, a relatively minor process. The cross section for this hydrogen-like species is also given by Equation (17), but the threshold energy is $h\nu_{He^+} = Z^2 h\nu_H = 54.4$ eV, and the cross-section at this threshold is $\sigma_{\nu_{He^+}} = \sigma_{\nu_H}/Z^2 = 1.6 \times 10^{-18}$ cm^{-2}. For the neutral helium photoionization cross-section, we use (Yan et al. 1998):

$$\sigma_{He}(\nu) = \frac{\sigma_a}{(h\nu/1 \text{ keV})^{7/2}} \left(1 + \sum_{n=1}^6 \frac{a_n}{(\nu/\nu_{He})^{n/2}}\right),$$
$$\nu > \nu_{He} \qquad (18)$$

where the threshold photon energy $h\nu_{He} = 24.6$ eV, $\sigma_a = 7.33 \times 10^{-22}$ cm^2, and the constants a_n are from Table 4 of Yan et al. (1998).

With the heating cross-section defined, we can now write the expression for ε_{max} in a more illustrative form:

$$\varepsilon_{max} = \frac{1}{R_p^2} \int_{R_p}^{R_{Roche}} r^2 \sum_i n_{i,r} \bar{\sigma}_{i,r} dr. \qquad (19)$$

The $n\sigma$ terms in the summation, which we will refer to as "heating coefficients," can be thought of analogously to absorption coefficients (e.g., Seager 2010). Thus, the efficiency of an isothermal wind cannot be greater than the normalized second moment of its total heating coefficient.

We note that Equation (19) gives us a simple way to compare the relative heating efficiencies of neutral hydrogen and helium. These processes will be similarly important for heating the atmosphere when the heating coefficients are comparable: $n_H \bar{\sigma}_H \sim n_{He} \bar{\sigma}_{He}$. In the high-energy limit, the cross-section for neutral helium photoionization is an order of magnitude larger than that for hydrogen photoionization, but there are also fewer helium atoms to ionize. We consider a 90–10 hydrogen–helium atmosphere that is optically thin, i.e., where $\exp(-\tau_{\nu,r}) \sim 1$ in Equation (16). In this case, the heating coefficients depend only on the assumed stellar spectrum. Stepping through the ensemble of stellar spectra collected by MUSCLES, we find that the optically thin heating coefficient for helium ranges from 20% (for ϵ Eri) to 67% (for GJ 1214) that of hydrogen. For a stellar spectrum similar to the M stars in the MUSCLES sample, helium photoionization can be a large (though still sub-dominant) heat source; pure-hydrogen escape models that have been developed for planets orbiting earlier stars may therefore underestimate the total thermospheric energy budget for planets orbiting M stars. K stars in this sample output relatively more flux near the hydrogen photoionzation threshold, so helium photoionization is a smaller heat source for planets orbiting K stars. These relative efficiencies are similar to those obtained from more detailed computational modeling (Salz et al. 2016a). These calculations are only meant to be illustrative; in general, the optical depth term $\exp(-\tau_{\nu,r})$ can be important, and the heating coefficients change substantially with radius.

2.3. Energetic Self-consistency

We next consider the implications of this upper limit on the mass loss efficiency for a photoionized isothermal Parker wind model, which parameterizes the density structure at the substellar point $n_{i,r}$ in terms of a mass-loss rate $\dot{M}$ and the outflow temperature T_0. For helium studies, the Parker wind is typically taken to be one-dimensional, but this greatly overestimates the work done. The wind is strongest at the substellar point because the irradiation is strongest there, but decreases in strength toward the terminator due to the diminished incident flux, and no wind is launched on the planetary nightside as the atmosphere is not irradiated there. This can be accounted for as follows: the planet is heated over only π steradians (Equation (13)), so the outflow is driven only over π steradians on the planetary dayside and the work done is decreased by a factor of $1/4$ compared to a 1D isotropically irradiated outflow (Stone & Proga 2009; Salz et al. 2016b).

Because the density distributions are functions of $\dot{M}$ and T_0 in this model, the energy-limited efficiency is itself a function of these parameters, and the mass-loss rate must satisfy:

$$\frac{\dot{M}}{4} \leqslant \frac{\varepsilon_{max}(\dot{M}, T_0)\pi R_p^3 F_{XUV}}{KGM_p}, \qquad (20)$$

where the factor of $1/4$ comes from the aforementioned 3D outflow geometry. Had we derived ε_{max} assuming an isotropically irradiated 1D outflow without this geometric factor, then we would be integrating over the entire planet in Equation (12), picking up a factor of 4 (the angular part of the integral would evaluate to 4π rather than π). Thus, the constraint on $\dot{M}$ would remain the same.

This inequality defines an allowed region on the $\dot{M}$–T_0 plane. The problem is fundamentally one of energetic self-

consistency: if we assume a mass-loss rate and thermosphere temperature, do the resulting density profiles allow enough heating to power the assumed mass-loss rate? For solutions outside the allowed region, the answer is no: they are not permitted unless there is some additional source of heat. Solutions on the boundary are exactly energy-limited; that is, they generate exactly enough heat to power their outflow. Solutions inside the boundary generate excess heat, which can always be balanced by additional cooling. If the cooling rate is known precisely, Equation (20) traces out a curve rather than an allowed region. We briefly consider this case in Appendix.

2.4. Regime of Validity

We note that our calculation is valid only for gas giant planets with H/He-rich envelopes and lower gravitational potentials experiencing (approximately) radially symmetric outflows. Detailed numerical simulations indicate that planets with gravitational potentials $\Phi_p \gtrsim 10^{13.1}$ erg g^{-1} exhibit strong temperature gradients, and cooling through Lyα and free–free emission becomes important (Salz et al. 2016a, 2016b). We have focused on isothermal, lossless outflows, so our model is therefore better suited to modeling lower gravity planets. High-gravity planets will still be governed by energy balance, but the isothermal Parker wind will not correctly describe the density distributions. We also note that H/He-rich Parker winds have been inadequate in predicting metastable helium signatures for sub-Neptunes thus far, which may indicate these planets differ substantially in composition from the pure H/He atmosphere assumed here (Kasper et al. 2020; Krishnamurthy et al. 2021). Therefore, we do not recommend using this methodology for planets with $R_p \lesssim 4R_\oplus$. These criteria are satisfied for $\sim 30\%$ of the ~ 1000 transiting exoplanets with measured masses and radii on the NASA Exoplanet Archive.

Our model additionally assumes an idealized geometry for the wind, and will be less accurate for outflows deviating from the assumed geometry. There are several factors that contribute to such deviations. Interactions between the planetary and stellar winds can sculpt the outflow into a comet-like tail (McCann et al. 2019; MacLeod & Oklopčić 2021; Wang & Dai 2021b), and we therefore expect the model to perform worse for planets orbiting young and/or exceptionally active stars. WASP-107 b orbits a relatively active star and has a strongly blueshifted helium line profile and strong post-egress absorption (Allart et al. 2019; Kirk et al. 2020; Spake et al. 2021), both signs of an asymmetric outflow. There were initially hints of a similar tail for WASP-69b (Nortmann et al. 2018). However, subsequent observations and modeling both indicate that this planet's outflow is relatively symmetric (Vissapragada et al. 2020; Wang & Dai 2021a). Simulations and observations of the transiting planet HD 63433c, which orbits a 440 Myr old star, indicate that it also has a comet-like tail (Zhang et al. 2021), and simulations of the young planet AU Mic b suggest the strong stellar wind should shape its outflow as well (Carolan et al. 2020), though helium has not yet been conclusively detected in its atmosphere (Hirano et al. 2020).

Magnetically controlled outflows are also expected to deviate from the idealized geometry in this work. Outflowing material near equatorial latitudes follow closed magnetic field lines falling back onto the planet, whereas material near the poles may escape (Adams 2011; Trammell et al. 2011, 2014; Owen & Adams 2014). However, it is presently unclear to what

extent magnetic fields may affect metastable helium observations, which have thus far been well-fit by models without magnetic fields. This may be because the planetary outflows are dominated by ram pressure rather than magnetic pressure within the metastable helium photosphere (Zhang et al. 2021).

3. Application to Metastable Helium Observations

To show how the constraints from our energy-limited model may be used in practice, we consider published observations of metastable helium absorption from HAT-P-11b, WASP-69b, and HAT-P-18b. These three planets have all been observed using narrowband photometry or low-resolution spectroscopy, which provide minimal information about the line shape. This means that when an isothermal Parker wind model is used to fit the measured absorption signal, there is a large degeneracy between the mass-loss rate and the assumed outflow temperature. This degeneracy can be broken with line-shape measurements of sufficiently high precision, which independently constrain the outflow temperature (e.g., dos Santos et al. 2021). However, the line shape can also vary when the absorbing region is not optically thin (Salz et al. 2018), and when the outflow itself kinematically broadens the line (Allart et al. 2019; Seidel et al. 2021; Wang & Dai 2021b). This means that line shape alone is an imperfect proxy for outflow temperature. Even if this was not the case, the signal-to-noise ratio of the measured line profile is often too low to provide a useful constraint on the outflow temperature (Lampón et al. 2020, 2021b).

In this section, we show that we can use the energy-limited framework to place an upper bound on the temperatures of these outflows, resulting in tighter constraints on the retrieved mass-loss rates from the Parker wind model. For each of the three planets considered here, we used the p-winds code (e.g., dos Santos et al. 2021) to calculate isothermal Parker wind models and compared those models to the observed metastable helium signal. p-winds is an open-source implementation of the model described by Oklopčić & Hirata (2018) and Lampón et al. (2020). We evaluated these models over a grid defined by $\dot{M} = 10^9$–10^{12} g s^{-1} and $T_0 = 5000$–$15{,}000$ K. The temperature grid roughly corresponds to the range of temperatures seen in self-consistent simulations (Salz et al. 2016b; Wang & Dai 2021a, 2021b). At each point on our grid, we computed the outflow density structure (for a 90/10 H/He composition) and calculated the corresponding ionization structure and level populations with p-winds. In these calculations, we noticed that the approximation for the hydrogen photoionization rate in Equation (9) of Oklopčić & Hirata (2018) tended to over-predict the rate close to the ionization front, which is consequential for the modeled mass-loss efficiency. We therefore updated the calculation in p-winds to avoid the approximation. We also note that our number density of ionized helium is overestimated because some of the ionized helium will end up populating He^{2+} in steady-state, which p-winds does not account for. By ignoring this minor (e.g., Salz et al. 2016b) sink, we obtain a slightly larger $\varepsilon_{\max}$ than we otherwise would.

We then used the framework from Section 2 to calculate the self-consistent $\dot{M}$–T_0 region for each planet. At each $(\dot{M}, T_0)$ wind on the grid, we integrated the density distributions of H and He to obtain column densities, from which we computed the total optical depth as a function of frequency and radius $\tau_{\nu,r}$. Using this optical depth, the cross sections in Equations (17)
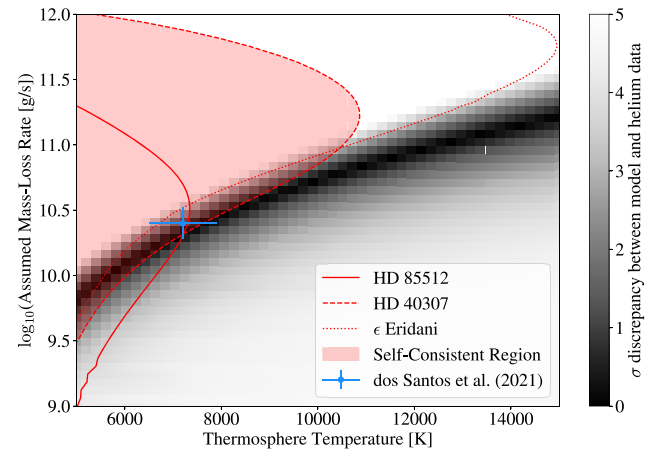

Figure 1. Mass-loss modeling for the HAT-P-11b observations presented in Mansfield et al. (2018). The black shading indicates the σ discrepancy between the mass-loss model in each grid cell and the metastable helium observation. The red shading indicates the self-consistent region from Equation (20) using the scaled spectrum of HD 40307, and the boundary for a perfectly energy-limited outflow assuming this spectrum is given with the dashed red line. The solid and dotted red lines give the boundary of the self-consistent regions for HD 85512 and ϵ Eridani, respectively. The blue point additionally indicates the 1σ range from the dos Santos et al. (2021) retrieval on the Allart et al. (2018) high-resolution spectrum.

and (18), the yield term in Equation (10), and the assumed stellar spectrum, we then calculated the heating cross-sections using Equation (16). Finally, we multiplied by the density distributions to get the heating coefficients, summed to get the total heating coefficient, and took the second moment to get the upper limit on the mass-loss efficiency per Equation (19). To assess whether or not a given outflow was self-consistent, we used this $\varepsilon_{\max}$ to calculate the maximum mass-loss rate via Equation (20). If we found a maximum mass-loss rate lower than the assumed mass-loss rate, the solution was energetically inconsistent; otherwise, it was admissible. This procedure has been added in v1.2.4 of the p-winds code.

3.1. HAT-P-11b

HAT-P-11b is slightly larger in mass and radius than Neptune ($\Phi_p \approx 3 \times 10^{12}$ erg g^{-1}), and orbits its K4 host star with a period of 5 days (Bakos et al. 2010). Mansfield et al. (2018) detected helium absorption in the atmosphere of this planet at low resolving power with Hubble Space Telescope WFC3/G102, and Allart et al. (2018) detected a comparable absorption signal at high resolving power with CARMENES. For this planet, the high signal-to-noise of the line shape measured by Allart et al. (2018) provides us with an independent measurement of the outflow temperature. dos Santos et al. (2021) fitted the line absorption profile from Allart et al. (2018) with a Parker wind model using the p-winds code and found that it was best matched by an outflow with $T_0 = 7200 \pm 700$ K and $\dot{M} = 2.5^{+0.8}_{-0.6} \times 10^{10}$ g s^{-1}. In this study we instead fitted the unresolved measurements from Mansfield et al. (2018), and used our energy-limited framework to help resolve the $\dot{M}$–T_0 degeneracy. We use the stellar spectrum of HD 40307 for this calculation, which is the same choice made by dos Santos et al. (2021).

We show the resulting constraints on the outflow rate and temperature in Figure 1, and compare these constraints to the result from dos Santos et al. (2021). We find that some of the
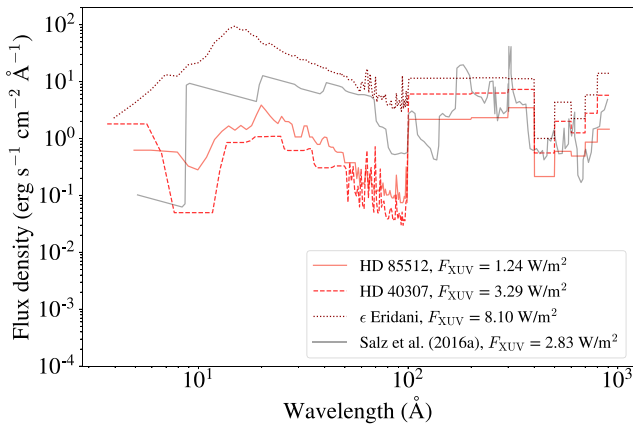
Figure 2. High-energy stellar spectra considered for HAT-P-11. All spectra have been scaled to the location of HAT-P-11b. Note that the Salz et al. (2016b) spectrum is binned differently than the three MUSCLES spectra.

Figure 3. Total number density of hydrogen (top) and number density of neutral hydrogen (bottom) for HAT-P-11b at the substellar point. Profiles from the Salz et al. (2016b) simulation are shown in blue, and our photoionized Parker wind model in red, with darker colors corresponding to higher temperatures.

previously reported Parker wind solutions with high temperatures and high mass-loss rates are in fact energetically inconsistent; i.e., they do not have enough H and He to power the outflow by photoionization. This allows us to partially resolve the degeneracy between mass-loss rate and thermosphere temperature: the outflow must be cooler than ∼10,000 K and relatively weak ($\dot{M} \lesssim 10^{11}$ g s^{-1}). Our results are in good agreement with dos Santos et al. (2021), and their retrieved value matches our energy-limited contour within the 1σ level. We therefore conclude that this outflow is energy-limited. This is also consistent with the simulations of Salz et al. (2016b), who explicitly modeled radiative cooling in HAT-P-11b's outflowing atmosphere and found it to be negligible.

We also quantify our sensitivity to the choice of high-energy stellar spectrum by overplotting the boundary of the self-consistent region calculated using scaled spectra for HD 85512, which is less energetic in the XUV than the HD 40307 spectrum, and ϵ Eridani which is more energetic in the XUV (see Figure 2). To be fully consistent, we also re-calculated the constraints from the Parker wind models with the same stellar spectrum. However, we found that this does not substantially change the range of mass-loss rates and temperatures that are consistent with the metastable helium data, as the stellar spectra have similar shapes at wavelengths longward of 100 Å. In Figure 1, we show that the range of self-consistent solutions is somewhat larger when we use ϵ Eridani as a proxy for the star's high energy spectrum, and smaller when we use HD 85512, reflecting the differences in XUV luminosities for these stars. A larger XUV intensity tends to increase ionization throughout the outflow (though this is also somewhat dependent on the spectral shape, see e.g., Guo & Ben-Jaffel 2016), leading to lower neutral densities, and thus smaller values of $\varepsilon_{\max}$ per Equation (19). However, this effect is sub-linear and does not compensate for the linear dependence on $F_{\rm XUV}$ in the expression for the maximum mass-loss rate in Equation (20), so larger XUV luminosities lead to larger self-consistent regions.

We can use the Salz et al. (2016b) simulation to explore the validity of the Parker wind model for this planet, as their model self-consistently predicts the temperature and density profiles at the substellar point. Their model suggests a mass-loss rate at the substellar point of $10^{10.89}$ g s^{-1}, which they divide by 4 to correct for the non-uniform radiation (as we do in Equation (20)) for a final mass-loss rate of $\dot{M}_{\rm sim} = 10^{10.29}$
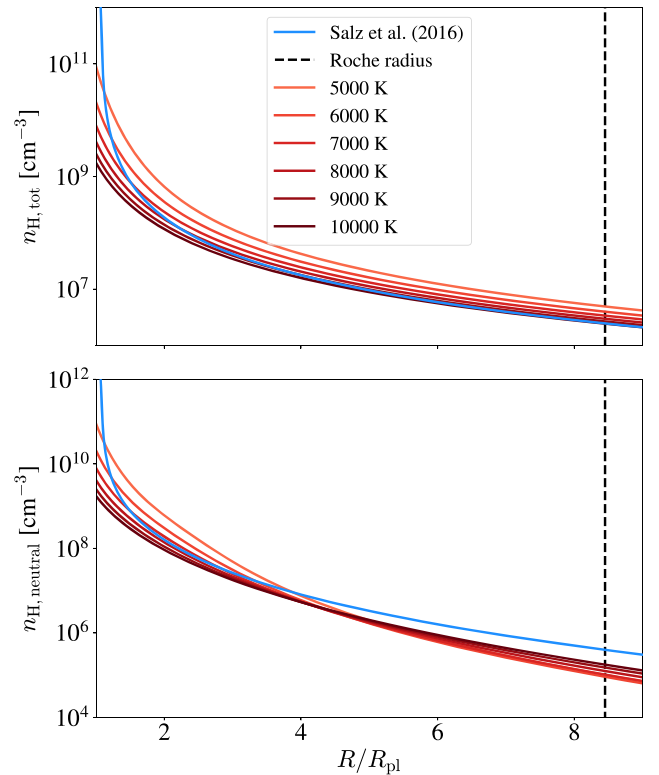
g s^{-1}. As we are comparing density profiles at the substellar point we selected isothermal Parker wind models with $\dot{M} = 10^{10.89}$ g s^{-1} and T_0 ranging from 5000 to 10,000 K in 1000 K steps. For the photoionization calculation we used the spectrum of HD 40307, which is closest to the spectrum used by Salz et al. (2016b). In Figure 3, we plot the total number density of hydrogen and the number density of neutral hydrogen from our models and compare it to the self-consistent simulations.

Throughout most of the outflow, the total hydrogen number densities agree quite well between the two models. They differ by orders of magnitude in total density near $R = R_{\rm p}$, but this is expected. The Parker wind model is a poor approximation for the lower atmosphere, but this region has a negligible effect on the predicted outflow. The high number density of hydrogen close to the planet leads to a very large optical depth near $R_{\rm p}$ so it does not contribute much to the heating budget in either model. Our model appears to give somewhat smaller number densities for neutral hydrogen near the Roche radius. This likely arises from our use of a K star spectrum from MUSCLES, whereas Salz et al. (2016b) used an inactive solar spectrum to reconstruct the shape of the spectrum in the EUV (see Figure 2). The discrepancy grows to about a factor of 2 at the Roche radius, but the densities here are small. Overall, the agreement between the two models is reasonable given the difference in methodology, and both models agree with the retrieval from dos Santos et al. (2021) for HAT-P-11b.
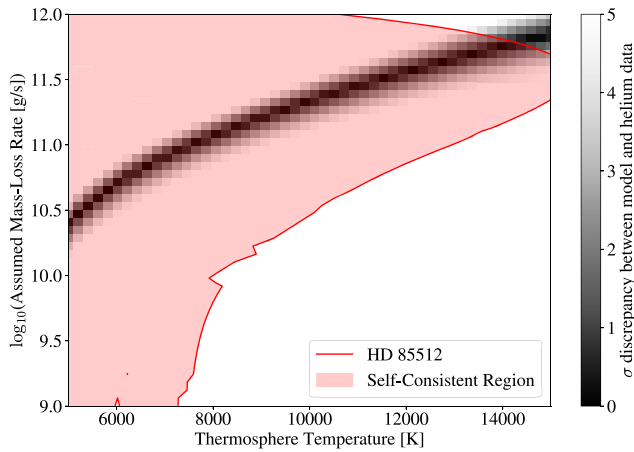
Figure 4. Same as Figure 1, but for the WASP-69b observations presented in Vissapragada et al. (2020).
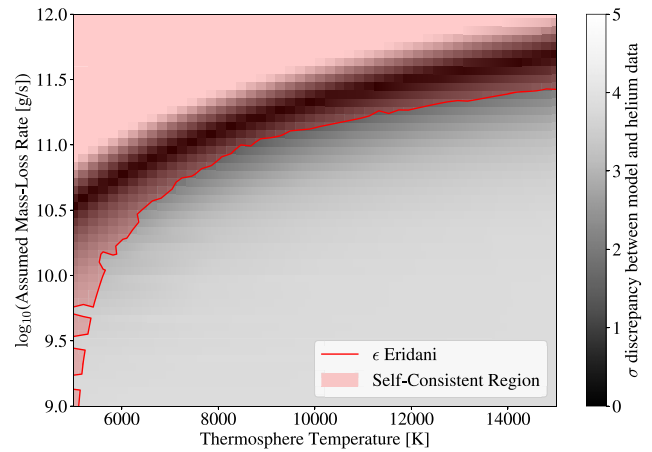

Figure 5. Same as Figure 1, but for the HAT-P-18b observations presented in Paragas et al. (2021).

3.2. WASP-69b

WASP-69b is a Neptune-mass, Jupiter-sized planet ($\Phi_p \approx 4 \times 10^{12}$ erg g^{-1}) in a 4 days orbit around a K5 host star (Anderson et al. 2014). The low density and large scale height of this planet, combined with the host star's favorable ratio of EUV to XUV flux (Oklopčić 2019), made it an ideal target for initial studies of mass loss with the metastable helium line. The helium absorption signal for this planet has been measured both spectroscopically (Nortmann et al. 2018) and photometrically (Vissapragada et al. 2020). In the latter work, we attempted to infer the mass-loss rate of WASP-69b using the Parker wind model from Oklopčić & Hirata (2018), and were able to place joint constraints on its mass-loss rate and thermosphere temperature.

In Figure 4, we show the energetically self-consistency region and compare it to the set of Parker wind models that match the metastable helium absorption reported in Vissapragada et al. (2020), using the stellar spectrum of HD 85512 as we did in that work. We find that the outflow must be cooler than 14,000 K and relatively weak ($\dot{M} \lesssim 10^{11.5}$ g s^{-1}). WASP-69b was also modeled self-consistently by Wang & Dai (2021a), who used a more sophisticated 3D approach coupling hydrodynamics and thermochemistry. These authors found that the data were best-matched by models with $\dot{M} \sim 10^{11}$ g s^{-1}, in agreement with our upper limit. The Wang & Dai (2021a) model also achieves a maximum temperature in the substellar direction of $\sim 10^4$ K, so (similarly to Lampón et al. 2020) we find that the isothermal Parker wind model agrees best with non-isothermal models near the maximum temperature.

3.3. HAT-P-18b

HAT-P-18b is a Jupiter-sized, Saturn-mass planet ($\Phi_p \approx 4 \times 10^{12}$ erg g^{-1}) orbiting a K2 dwarf with a period of 5.5 days (Hartman et al. 2011). In Paragas et al. (2021), we used narrowband photometry to detect helium absorption from an outflowing atmosphere with a significance of 4σ. In Figure 5, we fit the measurement from that work using our Parker wind model and compare the resulting contour to the energetically self-consistent region. For the XUV spectrum, we used the MUSCLES spectrum of the young K2 dwarf ϵ Eridani. Though HAT-P-18b is rather old $12.4^{+4.4}_{-6.4}$ Gyr (Hartman et al. 2011), it is quite active ($\log(R'_{HK}) = -4.73$; H. Isaacson 2022,

private communication), so ϵ Eridani ($\log(R'_{HK}) = -4.51$; Wright et al. 2004) is a reasonable choice of XUV proxy from the MUSCLES catalog.

For this planet, we could not limit the allowed mass-loss rate using energetics alone. The majority of models consistent with the helium data are also self-consistent. This is because the host star outputs a large XUV flux; as we discussed in Section 3.1, this tends to increase the number of self-consistent solutions with large mass-loss rates. More precise constraints on the mass-loss rate in this system will require precise line shape constraints from spectroscopic follow-up. The faintness ($J = 10.8$) of this system makes spectroscopic follow-up with CARMENES difficult, as its J magnitude is larger than the recommended magnitude limit for this instrument,[5] so line-shape measurements will require time on larger facilities like Keck II/NIRSPEC (e.g., Kirk et al. 2020; Spake et al. 2021).

4. Discussion and Conclusions

The isothermal Parker wind model is commonly used to interpret observations of metastable helium, with the ultimate goal of obtaining precise mass-loss rates for planets with observed helium absorption. However, there is a degeneracy between the outflow temperature and mass-loss rate in these models. The temperature can be constrained with spectroscopically resolved observations at high SNR, but remains a large source of uncertainty when fitting unresolved measurements and/or those at a lower SNR. We partially resolved this degeneracy by determining the maximum mass-loss efficiency of an isothermal wind driven by photoionization. We found that the efficiency is limited by a quantity we call the heating coefficient, which is the product of the number density and a weighted photoionization cross section, as described by Equation (19). We leveraged this constraint to show that a subset of the isothermal Parker wind models that agree with observations do not generate enough heat to remain energetically self-consistent. Outflows that generate just enough heat to remain self-consistent are exactly energy-limited, with the numerical value of the efficiency term depending on the assumed mass-loss rate, and outflows that generate excess heat must re-radiate some of their energy.

---

[5] https://carmenes.caha.es/ext/instrument/index.html

We re-examined published photometric and low-resolution spectroscopic observations of mass loss from HAT-P-11b, WASP-69b, and HAT-P-18b, which were originally fitted with a Parker wind model that allowed for a wide range of outflow temperatures and mass loss rates. We showed that the outflows from the former two planets must be relatively weak ($\dot{M} \lesssim 10^{11.5}$ g s^{-1}), but found that energetics could not further constrain the mass-loss rate for HAT-P-18b. Our results are in good agreement with more detailed numerical simulations of WASP-69b (Wang & Dai 2021a) and HAT-P-11b (Salz et al. 2016b), and additionally agree with complementary constraints on the outflow temperature of HAT-P-11b from line shape measurements (Allart et al. 2018; dos Santos et al. 2021). Furthermore, when line shape information is available (as it is for seven planets in the literature: HAT-P-11b, HAT-P-32b, WASP-69b, WASP-107b, HD 189733b, HD 209458b, and GJ 3470b) we can use our methodology to assess how close an outflow is to the energy limit. In this study, we showed that HAT-P-11b is experiencing an energy-limited outflow.

Our investigation revealed that the location of the self-consistent region on the $\dot{M}-T_0$ plane can shift in response to changing assumptions. First, as we showed in Figure 1, the extent of this region is sensitive to the assumed stellar spectrum; whenever possible, the spectra used in this model should be observationally calibrated. The models are also sensitive to the details of the photoionization calculation; any over- or under-estimation of the ionization fraction changes the self-consistent region. The assumed ratio of hydrogen to helium also matters, because the heating cross-section for neutral helium can be an order of magnitude larger than that for hydrogen for the late-type stars we considered in this work. Finally, the self-consistent region can move to higher temperatures if there are additional heat sources that are not included in the model. For instance, core-powered mass-loss (Ginzburg et al. 2016; Gupta & Schlichting 2019, 2020, 2021) could provide additional luminosity on the right-hand side of Equation (6).

In addition to refining the inferred mass-loss rates from metastable helium observations, our energetics framework also allows us to more generally elucidate the connection between the mass-loss efficiency in the energy limit and the outflow photophysics. This can be important when considering other potential heat sources. For example, Howe et al. (2020) studied the potential heating from photodissociation of molecular hydrogen and found that it was a sub-dominant outflow driver when ε was fixed to 0.1. Although our framework is imperfect for considering molecular winds, as there are more sources of heating and cooling to consider (Glassgold & Najita 2015; Salz et al. 2016b), we can nonetheless use it to explore what happens when we relax the assumption of fixed efficiency. The cross-section for molecular hydrogen photodissociation is resonant at the frequencies of Lyman–Werner transitions (e.g., Heays et al. 2017), causing the gas to self-shield. This means that the optical depth to dissociating photons will quickly exceed unity in the outer region of the outflow, greatly reducing the heating rate per Equation (15) inside a thin photodissociated region (Draine & Bertoldi 1996). We conclude that self-shielding may cause ε to be even lower than assumed by Howe et al. (2020).

Population-level surveys of present-day mass loss are increasingly within reach. As the body of published helium absorption signals continues to grow, it is important to develop models that allow us to quickly and uniformly infer mass-loss rates from a large sample of observations. Our new outflow energetics framework can be used to enhance the scientific output of these surveys by providing more precise constraints on the retrieved mass-loss rates without significant computational expense. Although this method is currently limited to lower gravity planets, it could be extended to higher gravities in future studies by using simple prescriptions for the density structures and cooling rates of non-isothermal outflows. Despite this limitation, our framework can already be used to model helium signals from low-gravity, H/He-rich planets, like those in and near the Neptune desert. Helium observations have the potential to provide the first population-level constraints on the predicted mass-loss rates for these enigmatic planets.

Appendix
Non-negligible Cooling

In the recombination limit, cooling becomes important (Murray-Clay et al. 2009; Owen & Alvarez 2016; Lampón et al. 2021a), and the approximation we made in Equation (6) greatly overpredicts the efficiency. We can repeat the calculation without making that assumption. When the cooling rate Λ can be written exactly, the efficiency is:

$$\varepsilon_{\mathrm{RL}} = \frac{1}{R_{\mathrm{p}}^2} \int_{R_p}^{R_{\mathrm{Roche}}} r^2 \sum_i n_{i,r} \bar{\sigma}_{i,r} dr - \frac{4}{R_{\mathrm{p}}^2} \frac{1}{F_{\mathrm{XUV}}} \int_{R_{\mathrm{p}}}^{R_{\mathrm{Roche}}} \Lambda r^2 dr,$$

(A1)

where the factor of four in the numerator of the cooling term reflects the fact that the planet can cool through all 4π steradians. Typically, Lyα is taken to be the dominant coolant for the outflow, in which case the cooling rate can be written:

$$\Lambda = C \left(\frac{n_{\mathrm{H}^+,r}}{\mathrm{cm}^{-3}} \right) \left(\frac{n_{\mathrm{H},r}}{\mathrm{cm}^{-3}} \right) \exp(-T_{\mathrm{c}}/T_0),$$

(A2)

where $n_{\mathrm{H}^+,r}$ is the number density profile of ionized hydrogen, $n_{\mathrm{H},r}$ is that of neutral hydrogen, $C = 7.5 \times 10^{-19}$ erg s^{-1} cm^{-3}, and $T_c = 118{,}348$ K (Black 1981; Murray-Clay et al. 2009; Owen & Alvarez 2016). Rather than tracing out a permitted region on the $\dot{M}-T_0$ plane as in Equation (19), Equation (A1) traces out a single curve of allowed solutions because the cooling is specified exactly. There are, however, many other cooling processes to consider even in a H/He gas including helium line emission, hydrogen and helium recombination

cooling, and free–free emission (Black 1981; Salz et al. 2016b). Additionally, our fundamental assumption of an isothermal wind is more readily violated for planets in the recombination limit when wind-launching is treated self-consistently (Salz et al. 2016b). For these reasons, our framework is ill-suited to exactly treat planets with strong cooling, and we default to the upper-limit formulation in Equation (20).

ORCID iDs

Shreyas Vissapragada ⓘ https://orcid.org/0000-0003-2527-1475

Heather A. Knutson ⓘ https://orcid.org/0000-0002-5375-4725

Leonardo A. dos Santos ⓘ https://orcid.org/0000-0002-2248-3838

Lile Wang ⓘ https://orcid.org/0000-0002-6540-7042

Fei Dai ⓘ https://orcid.org/0000-0002-8958-0683

References

Adams, F. C. 2011, ApJ, 730, 27
Allart, R., Bourrier, V., Lovis, C., et al. 2018, Sci, 362, 1384
Allart, R., Bourrier, V., Lovis, C., et al. 2019, A&A, 623, A58
Anderson, D. R., Collier Cameron, A., Delrez, L., et al. 2014, MNRAS, 445, 1114
Astropy Collaboration, Price-Whelan, A. M., Sipőcz, B. M., et al. 2018, AJ, 156, 123
Astropy Collaboration, Robitaille, T. P., Tollerud, E. J., et al. 2013, A&A, 558, A33
Black, J. H. 1981, MNRAS, 197, 553
Carolan, S., Vidotto, A. A., Plavchan, P., et al. 2020, MNRAS, 498, L53
dos Santos, L. A., Vidotto, A. A., Vissapragada, S., et al. 2021, arXiv:2111.11370
Draine, B. T., & Bertoldi, F. 1996, ApJ, 468, 269
Erkaev, N. V., Kulikov, Y. N., Lammer, H., et al. 2007, A&A, 472, 329
France, K., Loyd, R. O. P., Youngblood, A., et al. 2016, ApJ, 820, 89
Fulton, B. J., & Petigura, E. A. 2018, AJ, 156, 264
Fulton, B. J., Petigura, E. A., Howard, A. W., et al. 2017, AJ, 154, 109
Gaidos, E., Hirano, T., Mann, A. W., et al. 2020a, MNRAS, 495, 650
Gaidos, E., Hirano, T., Wilson, D. J., et al. 2020b, MNRAS, 498, L119
Ginzburg, S., Schlichting, H. E., & Sari, R. 2016, ApJ, 825, 29
Glassgold, A. E., & Najita, J. R. 2015, ApJ, 810, 125
Guo, J. H., & Ben-Jaffel, L. 2016, ApJ, 818, 107
Gupta, A., & Schlichting, H. E. 2019, MNRAS, 487, 24
Gupta, A., & Schlichting, H. E. 2020, MNRAS, 493, 792
Gupta, A., & Schlichting, H. E. 2021, MNRAS, 504, 4634
Hardegree-Ullman, K. K., Zink, J. K., Christiansen, J. L., et al. 2020, ApJS, 247, 28
Harris, C. R., Millman, K. J., van der Walt, S. J., et al. 2020, Natur, 585, 357
Hartman, J. D., Bakos, G. Á., Sato, B., et al. 2011, ApJ, 726, 52
Heays, A. N., Bosman, A. D., & van Dishoeck, E. F. 2017, A&A, 602, A105
Hirano, T., Krishnamurthy, V., Gaidos, E., et al. 2020, ApJL, 899, L13
Howe, A. R., Adams, F. C., & Meyer, M. R. 2020, ApJ, 894, 130
Hunter, J. D. 2007, CSE, 9, 90
Kasper, D., Bean, J. L., Oklopčić, A., et al. 2019, AJ, 160, 258
Kirk, J., Alam, M. K., López-Morales, M., et al. 2019, AJ, 159, 115
Krenn, A. F., Fossati, L., Kubyshkina, D., et al. 2021, A&A, 650, A94
Krishnamurthy, V., Hirano, T., Stefánsson, G., et al. 2021, AJ, 162, 82
Kubyshkina, D., Fossati, L., Erkaev, N. V., et al. 2018, ApJL, 866, L18
Lamers, H. J. G. L. M., & Cassinelli, J. P. (ed.) 1999, Introduction to Stellar Winds, 452 (Cambridge: Cambridge Univ. Press), 452
Lampón, M., López-Puertas, M., Czesla, S., et al. 2021a, A&A, 648, L7
Lampón, M., López-Puertas, M., Lara, L. M., et al. 2020, A&A, 636, A13
Lampón, M., López-Puertas, M., Sanz-Forcada, J., et al. 2021b, A&A, 647, A129
Lopez, E. D., & Fortney, J. J. 2013, ApJ, 776, 2
Loyd, R. O. P., France, K., Youngblood, A., et al. 2016, ApJ, 824, 102
MacLeod, M., & Oklopčić, A. 2021, arXiv:2107.07534
Mansfield, M., Bean, J. L., Oklopčić, A., et al. 2018, ApJL, 868, L34
McCann, J., Murray-Clay, R. A., Kratter, K., et al. 2019, ApJ, 873, 89
Murray-Clay, R. A., Chiang, E. I., & Murray, N. 2009, ApJ, 693, 23
Ninan, J. P., Stefansson, G., Mahadevan, S., et al. 2020, ApJ, 894, 97
Nortmann, L., Pallé, E., Salz, M., et al. 2018, Sci, 362, 1388
Oklopčić, A. 2019, ApJ, 881, 133
Oklopčić, A., & Hirata, C. M. 2018, ApJL, 855, L11
Osterbrock, D. E., & Ferland, G. J. (ed.) 2006, Astrophysics of Gaseous Nebulae and Active Galactic Nuclei (2nd ed.; Sausalito, CA: Univ. Science Books)
Owen, J. E. 2019, AREPS, 47, 67
Owen, J. E., & Adams, F. C. 2014, MNRAS, 444, 3761
Owen, J. E., & Alvarez, M. A. 2016, ApJ, 816, 34
Owen, J. E., & Jackson, A. P. 2012, MNRAS, 425, 2931
Owen, J. E., & Wu, Y. 2013, ApJ, 775, 105
Owen, J. E., & Wu, Y. 2017, ApJ, 847, 29
Paragas, K., Vissapragada, S., Knutson, H. A., et al. 2021, ApJL, 909, L10
Salz, M., Czesla, S., Schneider, P. C., et al. 2016a, A&A, 586, A75
Salz, M., Czesla, S., Schneider, P. C., et al. 2018, A&A, 620, A97
Salz, M., Schneider, P. C., Czesla, S., et al. 2016b, A&A, 585, L2
Seager, S. (ed.) 2010, Exoplanet Atmospheres: Physical Processes (Princeton, NJ: Princeton Univ. Press)
Seidel, J. V., Ehrenreich, D., Allart, R., et al. 2021, A&A, 653, A73
Shematovich, V. I., Ionov, D. E., & Lammer, H. 2014, A&A, 571, A94
Spake, J. J., Oklopčić, A., & Hillenbrand, L. A. 2021, AJ, 162, 284
Spake, J. J., Sing, D. K., Evans, T. M., et al. 2018, Natur, 557, 68
Stone, J. M., & Proga, D. 2009, ApJ, 694, 205
Bakos, G. Á., Torres, G., Pál, A., et al. 2010, ApJ, 710, 1724
Trammell, G. B., Arras, P., & Li, Z.-Y. 2011, ApJ, 728, 152
Trammell, G. B., Li, Z.-Y., & Arras, P. 2014, ApJ, 788, 161
Van Eylen, V., Agentoft, C., Lundkvist, M. S., et al. 2018, MNRAS, 479, 4786
Vidal-Madjar, A., Désert, J.-M., Lecavelier des Etangs, A., et al. 2004, ApJL, 604, L69
Vidal-Madjar, A., Lecavelier des Etangs, A., Désert, J.-M., et al. 2003, Natur, 422, 143
Virtanen, P., Gommers, R., Oliphant, T. E., et al. 2020, NatMe, 17, 261
Vissapragada, S., Knutson, H. A., Jovanovic, N., et al. 2020, AJ, 159, 278
Wang, L., & Dai, F. 2021a, ApJ, 914, 98
Wang, L., & Dai, F. 2021b, ApJ, 914, 99
Watson, A. J., Donahue, T. M., & Walker, J. C. G. 1981, Icar, 48, 150
Wright, J. T., Marcy, G. W., Butler, R. P., et al. 2004, ApJS, 152, 261
Yan, F., & Henning, T. 2018, NatAs, 2, 714
Yan, M., Sadeghpour, H. R., & Dalgarno, A. 1998, ApJ, 496, 1044
Zhang, M., Knutson, H. A., Wang, L., et al. 2021, AJ, 161, 181